Energy Engineering

Tech Science Press

DOI: 10.32604/ee.2023.029620

ARTICLE

Analysis of Sub-Synchronous Oscillation of Virtual Synchronous Generator and Research on Suppression Strategy in Weak Grid

Chongyang Zhao, Wei Chai, Beibei Rui and Lin Chen*

Jianbi Power Plant of National Energy Group, Zhenjiang, 21200, China

*Corresponding Author: Lin Chen. Email: cl20220920@126.com

Received: 16 December 2022 Accepted: 13 April 2023 Published: 31 October 2023

ABSTRACT

At present, the direct drive permanent magnet synchronous generator (DD-PMSG) grid connected system based on virtual synchronous generator (VSG) control will experience power oscillation at sub synchronous frequencies. The mechanism and characteristics of this new type of sub-synchronous interaction (SSI) are not yet clear, and the system cannot recover to steady state solely based on the characteristics of VSG itself. Especially when connected to a weak current network, oscillations are more pronounced, affecting the stability of the system. In severe cases, the system may trigger shutdown protection and be disconnected from the network. Existing research has only analyzed the oscillation mechanism under this phenomenon and has not proposed corresponding control strategies. This article proposes a VSM control strategy based on the VSG control algorithm, which balances the dq axis component of voltage and current, and improves the voltage and current loop of VSG control to reduce the impact of sub-synchronous oscillation (SSO) on the power grid. In MATLAB/Simulink, a simulation model of the proposed control strategy was built to verify its correctness and effectiveness.

KEYWORDS

PMSG; VSG; subsynchronous oscillation; impedance modelling

Nomenclature

COA	Chaotic optimization algorithm
DD-PMSG	Direct-drive permanent magnet synchronous generator
DFIG	Doubly fed induction generator
ECKF	Extended complex Kalman filter
FACTS	Flexible AC transmission system
GSC	Grid-side converter
HVDC	High-voltage direct current
IGE	Inductive generator effect
IMM	Interactive multi-model
ML	Maximum likelihood
MRF	Median regression function
NFs	Notch filters
PLL	Phase-locked loop
PMSG	Permanent magnet synchronous generator

PMU	Phasor measurement unit
PSO	Particle swarm optimization
RSC	Rotor-side converter
SCR	Short-circuit ratio
SG	Synchronous generator
SMES	Superconducting magnetic energy storage
SSCI	Sub-synchronous Control Interaction
SSDC	Sub-synchronous damping controller
SSI	Sub-synchronous interaction
SSO	Sub-synchronous oscillation
SSR	Sub-synchronous resonance
STATCOM	Static synchronous compensator
SVC	Static reactive power compensator
TA	Transient torque amplification
TI	Torsional interaction
VSC	Voltage source converter
VSG	Virtual synchronous generator

1 Introduction

By the end of 2021, China's installed capacity of power generation was 2,200.58 million kilowatts (MWs), which increases by 9.5% over the end of last year. Among them, the installed capacity of thermal power and hydropower increased by 4.7% and 3.4%, respectively; the installed capacity of grid-connected wind power was 281.53 MWs, which increases by 34.6%; the installed capacity of grid-connected solar power was 253.43 MWs, an increase of 24.1% [1]. It can be seen that the installed capacity of thermal power and hydropower has increased significantly, and the installed capacity of grid-connected wind power and solar power has grown rapidly. Unfortunately, with the rapid growth of wind power, sub-synchronous oscillations (SSO) have been observed in some wind farms with weak grid interconnection. SSO greatly affects the stability of the system, and in severe cases, the system may trigger shutdown protection and be disconnected from the network. This article analyzes the SSO phenomenon caused by the direct drive wind power grid-connected system passing through long-distance transmission lines. On the one hand, we suppress the impact of SSO on the power grid, and on the other hand, we improve the performance of VSG under frequency oscillation.

In recent years, virtual synchronous generator (VSG) technology [2] has been used to control grid-connected inverters. It borrows the mechanical and electromagnetic equations from the SG [3] while combining inertia characteristics [4], active power regulation frequency [5] and reactive power regulation voltage [6]. However, VSGs borrowed from SG will also have all the advantages and disadvantages of synchronous machines, such as the possibility of bad phenomena in synchronous inverters; loss of stability due to under-excitation and oscillations [7].

In the steady-state or small disturbance of the power system, the oscillation of the traditional power system is mainly divided into the low-frequency oscillation (0.5∼3 Hz) and the SSO (<50 Hz) of the local generator and external network [8]. With the increasing proportion of power electronic equipment in the power system, the broadband oscillation of modern power systems is mainly divided into resonance and control oscillation. The resonance dominated by power electronic equipment is caused by the generation and transmission of new energy, while the control oscillation is caused by the integration of new energy into the grid. Two types of oscillations will be briefly described below:

(1) Resonant class oscillations are caused by inductive-capacitive LC resonant circuits. This oscillation contains three subclasses: conventional sub-synchronous resonance (SSR), ferromagnetic resonance, and power electronics-dominated resonance. Based on the destabilization mechanism, conventional SSR can be further classified into induction generator effect (IGE), torsional interaction (TI) and transient torque amplification (TA). Ferromagnetic resonance is a form of self-excited oscillation in power systems and is a resonant phenomenon generated by the nonlinear inductance of transformers, voltage transformers and other components in substations, as well as the grounding capacitance of cables and overhead lines. Main resonances in power electronics include high frequency resonances in flexible DC transmission systems, resonances in doubly-fed turbines through series complementary feeder systems, and high frequency switching or control triggered resonances in voltage source converters (VSCs).

(2) For control oscillations, there is no LC electrical resonance loop in the system and the power electronic controller has a significant influence on such oscillations. This type of oscillation includes two subcategories of SSO and power electronic dominated control oscillations. Conventional SSO refers to the sub-synchronous oscillation phenomenon caused by the interaction between the synchronous generator shaft system and the fast control characteristics of the power electronics of high-voltage direct current (HVDC) or flexible AC transmission systems (FACTS) [9,10]. The dynamic interaction between the VSC equipment and the weak grid causes the direct-drive wind power control system to exhibit negative damping of the sub-synchronous oscillation mode, which triggers the sub/super-synchronous oscillation phenomenon. In large-scale new energy sites, SSO with time-varying frequencies can be monitored by means of series complementary or weak AC grid systems [11,12]. This phenomenon is related to the converter control and line series complement capacitance of the doubly-fed induction wind turbine and is not related to the shaft torsional oscillation and is referred to as sub-synchronous Control Interaction (SSCI). Some studies have shown that there is also SSCI between the VSG and the weak power grid [13]. Reference [14] presented a literature review on the damping of power system oscillations. The study identifies various control design techniques, technologies and features used in power systems. In addition, it discusses various devices and tools for minimizing damping in conventional grids and renewable energy sources.

With the frequent occurrence of oscillations, online monitoring and accurate alarming of the power system are essential for its safe and stable operation. A phasor measurement unit (PMU) enables dynamic real-time monitoring of the power system [15]. However, where the use of series capacitors in long-distance transmission lines can lead to SSO, the SSO phenomenon must be accurately detected within a short time. An efficient, safe and improved method of SSO detection based on voltage signals is proposed, where the voltage magnitude signal is passed through a first order bandpass filter only via a sub-synchronous frequency and the best decision is made in the decision phase (single sign-on detection, immediate tripping or normal tripping) based on the data received from the analysis phase [16].

The traditional power system oscillation problems have more mature theories and methods in terms of mechanism research, characteristic analysis and oscillation suppression. However, in the new power system, the broadband oscillations caused by power electronics present new phenomena and characteristics, such as various forms, broadband characteristics, time-varying characteristics and wide-area propagation characteristics. A new strategy for suppressing SSO in series capacitor compensated power systems by controlling the active power of superconducting magnetic energy storage (SMES) devices was proposed in [17]. The strategy is based on the generator acceleration signal and the chaotic optimization algorithm (COA) is used to obtain the optimal parameters of the proposed controller. However, reactive power is not taken into account. Reference [18] proposed

a method to control the active and reactive power of a SMES system based on reference [17], which prioritises active power over reactive power, with primary frequency and voltage control used to calculate active and reactive power reference values for the SMES system, and these gains are calculated by a particle swarm optimization (PSO) algorithm. A median regression function (MRF) based state estimation method was proposed in reference [19]. The algorithm uses an interactive multi-model (IMM)-based fusion architecture deployed on each monitoring node. The system considers an exogenous variable-driven representation of the state. Initial regression analysis based on mapping functions is used to describe the state estimation bounds at the time of data injection. An improved PLL was proposed to replace the conventional phase-locked loop in reference [20]. Aiming at the problem that the control of the rotor-side converter (RSC) and grid-side converter (GSC) in the doubly fed induction generator (DFIG) wind power system is disturbed by harmonic signals under SSO, it is proposed to add the quasi-resonance controller to the RSC and GSC to suppress SSO. However, both traditional PI control and quasi-resonant controllers have the problem of insufficient robustness. To reduce the SSO of the permanent magnet synchronous generator (PMSG), an energy shaping L2 gain controller (ESLGC) for the MSC and the GSC was proposed in reference [20]. This ESLGC has better robustness and damping performance under various operating conditions. However, ESLGC does not use non-linear analysis techniques to assess the performance of the damping controller, which has resulted in less widespread use. Several scholars have investigated the use of static reactive power compensators (SVCs) and TCR-FCs (silicon controlled rectifiers with fixed capacitors) to suppress SSO [21]. The collection of reactive power variations, frequency variations, active power variations and current variations can be used to enhance the dynamic response of the system. However, Reference [21] only captures reactive power changes and does not further combine the two signals into a single controller. Similarly, a new auxiliary sub-synchronous damping controller (SSDC) has been proposed for transmission lines with series compensation [22] and an auxiliary SSDC for static synchronous compensator (STATCOM), which uses the generator rotor speed deviation signal as a stabilising signal [23]. In contrast to reference [22], MMC-STATCOM proposes an additional broadband damping controller that provides an additional broadband damping control strategy to mitigate SSCI. This method uses notch filters (NFs) to filter only the fundamental frequency component of the current to obtain the corresponding sub-synchronous component to generate the damping control signal [24]. This strategy does not require phase compensation and, in contrast to previous studies, always allows the extraction of the corresponding sub-synchronous components. For SSO caused by weak grids, an impedance model of VSG under weak grids was developed and the mechanism and characteristics of the occurrence of sub-synchronous resonance (SSR) in the analysis [25]. Using small-signal analysis [26,27], key parameters such as the PLL were examined. References [28,29] improved the existing extended complex Kalman filter (ECKF) technique to track electromechanical oscillations using simultaneous phase measurements. Not only can the distributed structure be estimated to estimate the oscillation parameters of the local substation, but also the ability to detect multiple oscillations with similar frequencies can be improved.

In summary, there are many new challenges to study and analyze SSO. Table 1 lists the current mainstream studies on suppressing SSO, and in response to the shortcomings of the above studies, this paper considers the frequency coupling effect and uses VSM-VSG cooperative control to effectively suppress SSO and provide frequency support for the system.

Table 1: Comparison of research methods

Analysis and research	Advantage	Disadvantage	Ref.
Sub-synchronous damping controller	1. Simple structure	1. Poor control performance	[21–23,30,31]
Adaptive mitigation scheme	1. Reshape the impedance response of the system	1. Slow response	[32]
Self-regulating VSG control system	1. Provide frequency support 2. Suppress transient in stator current 3. Adaptive estimation of power grid impedance	1. VSG control algorithm is only used for network side control	[33–35]
A virtual coupling suitable for DFIG	1. The use of virtual couplings	1. Suppress the oscillation of the traditional SSO turbine side motor shaft	[36]
Parameter recognition algorithm	1. Obtain frequency, amplitude and phase of the fundamental frequency, sub-synchronous and supers-synchronous components	1. The complexity of algorithmic control	[17–19,37]
Impedance modelling	1. Clearly corresponds to the control loop 2. The established positive sequence impedance and negative sequence impedance can be verified through simulation and testing	1. Neglected machine side dynamics and DC side perturbations	[25,38,39]

This study uses an analytical model of a type IV wind power system on a weak current network to demonstrate sub-synchronous frequency oscillations. Firstly, considering the frequency coupling effect, impedance model analysis is conducted on VSG. The purpose of drawing a Bode diagram is to examine key factors and determine the root causes of such instability and resonance problems. To improve the SSO suppression ability of VSG, the application of VSM control strategy on the machine side and a new voltage and current dual loop control strategy on the network side were studied. This control strategy improves the grid connection voltage and current waveform by adding the dq component of the grid voltage to the GSC, in order to meet the requirements of harmonic suppression under different weak current grid conditions. The simulation results show that this method can effectively suppress the impact of SSO on the power grid.

The main contributions of this paper are summarized below:

1. VSG impedance model was analyzed based on frequency coupling effect and DC side disturbance to study the influence of VSG parameters on SSO suppression.

2. Use the VSM control policy to increase damping and inertia during the oscillation period to provide frequency support for the system. The dq axis components of voltage and current are balanced by adding the dq component of grid voltage to the GSC side to form feedback.

The current dissertation organization is continued. Section 2 presents the general principles of the VSG control technique. Section 3 presents the complete Type IV wind power model. Section 4 models the impedance of the PLL and VSG. Section 5 presents the effect of the parameters of impedance modelling on the bode plots and the results of adopting the suppression strategy. Section 6 is the conclusion.

2 VSG Control Principle

The classic control block diagram of VSG is shown in Fig. 1, where U_{dc} is the DC bus voltage, $S_1 \sim S_6$ are insulated gate bipolar transistors (IGBTs), and L_f, R_f, L_g, R_g, and C_f are LCL filter parameters. The structure is a full-bridge inverter with a three-phase, three-wire system. The output voltage u_{abc} and current i_{abc} of the VSG are sampled in real-time to calculate the actual output power, and the output modulation wave E is obtained by using the VSG control algorithm. Then, the modulating wave E^* of the current loop is obtained through the virtual impedance function. The current loop affects the SVPWM modulation wave according to the input voltage E^*, thereby controlling the output voltage from VSG and achieving precise control of the system.

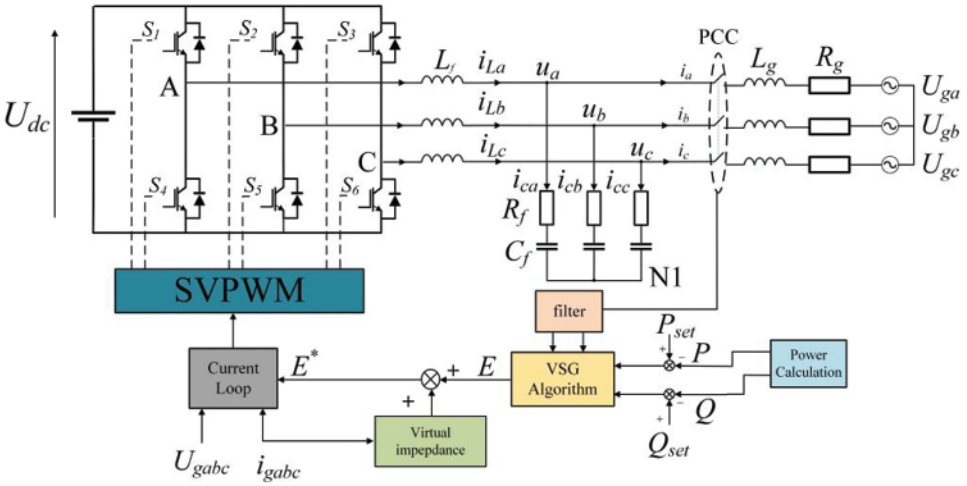

Figure 1: VSG-class control block diagram

The traditional SGs adjust the active output of the generator by adjusting the mechanical torque and realising the response to the frequency deviation of the grid through the frequency regulator. Based on this principle, the adjustment of the active command of the grid-connected inverter is realized by adjusting the virtual mechanical torque T_m of the VSG. The prime mover regulation and the rotor equation of motion together constitute the power frequency regulator. The synchronous generator prime mover is adjusted as:

$$J\frac{d\omega}{dt} = T_m - T_e - T_d = T_m - T_e - D(\omega - \omega_0) \tag{1}$$

$$Q_{set} + D_q (V_0 - V) - Q_e = K_s E_m \tag{2}$$

$$\frac{d\delta}{dt} = \omega - \omega_n \tag{3}$$

$$P_m = P_{ref} + k_f (\omega_n - \omega) \tag{4}$$

where P_m is the mechanical power, ω is the angular frequency, δ is the power angle, ω_0 is the grid synchronous angular velocity, P_{ref} is the given electromagnetic (active) power, and K_f is the frequency modulation coefficient. T_m, T_e and T_d are the mechanical, electromagnetic and damping torques of the SG, respectively, D is the frequency-active power droop coefficient, and J is the moment of inertia of the SG.

Furthermore, the potential voltage vector of the VSG can be obtained as:

$$E = \begin{bmatrix} e_a \\ e_b \\ e_c \end{bmatrix} = \begin{bmatrix} E\sin(\varphi) \\ E\sin(\varphi - 2\pi/3) \\ E\sin(\varphi + 2\pi/3) \end{bmatrix} \tag{5}$$

where $\varphi = \int \omega dt$ is the phase of the VSG.

As shown in Fig. 1, the relationship between the internal potential of the VSG, the output terminal voltage and the output current can be as follows:

$$\begin{bmatrix} e_a \\ e_b \\ e_c \end{bmatrix} = \left(\frac{L_f C_f s^2}{1 + C_f R_f s} + 1 \right) \begin{bmatrix} u_a \\ u_b \\ u_c \end{bmatrix} + L_f s \begin{bmatrix} i_a \\ i_b \\ i_c \end{bmatrix} \tag{6}$$

3 Impedance Modelling

Under the disturbance of small signal, the voltage and current of the AC port of the converter contain the fundamental frequency component, the disturbance frequency component and the coupling frequency component. Taking phase A as an example, the time domain expressions of voltage and current of the converter port are, respectively:

$$\begin{aligned} u_a(t) = {} & U_1 \cos(2\pi f_1 t + \phi_{u1}) \\ & + U_p \cos\left(2\pi f_p t + \phi_{up}\right) + U_n \cos(2\pi f_n t + \phi_{un}) \end{aligned} \tag{7}$$

$$\begin{aligned} i_a(t) = {} & I_1 \cos(2\pi f_1 t + \phi_{i1}) \\ & + I_p \cos\left(2\pi f_p t + \phi_{ip}\right) + I_n \cos(2\pi f_n t + \phi_{in}) \end{aligned} \tag{8}$$

where the fundamental frequency voltage and current amplitudes are U_1, I_1 and the initial phase is set to zero, the subscript p is used to represent the component with frequency f_p, and the subscript n is used to represent the component with frequency f_n.

Fourier transforms the corresponding time-domain expressions of Eqs. (7) and (8) into:

$$U_a[f] = \begin{cases} U_1 & f = \pm f_1 \\ U_p & f = \pm f_p \\ U_n & f = \pm f_n \end{cases} \tag{9}$$

$$I_a[f] = \begin{cases} I_1 & f = \pm f_1 \\ I_p & f = \pm f_p \\ I_n & f = \pm f_n \end{cases} \tag{10}$$

where $U_1 = \frac{1}{2}U_1$, $U_p = \frac{1}{2}U_p e^{\pm j\phi up}$, $U_n = \frac{1}{2}U_n e^{\mp j\phi un}$ and the current components I_1, I_p, and I_n are similar to the voltages.

3.1 DC Link

The new energy and grid interconnection system can be simplified in Fig. 2. The DC link is mainly composed of capacitors, which stabilize the DC voltage rectified by the machine-side rectifier at a fixed value.

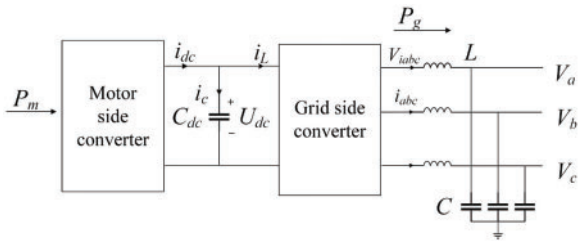

Figure 2: DC link structure diagram

In Fig. 2, P_m is the instantaneous power output by the machine, and P_g is the absorbed power of the power grid. The MSC converts the AC output of the motor into DC power. After the DC voltage has passed through the GSC, it is then converted to AC power with the same frequency, amplitude and phase as the grid voltage. As can be seen from Fig. 2. The energy storage of the capacitor C_{dc} is:

$$\frac{C_{dc}}{2}\frac{d\left(U_{dc}\right)^2}{dt} = P_m - P_g \tag{11}$$

In order to effectively transmit power, U_{dc} should be controlled as a constant.

It can be seen from the power balance that the power output at the machine side should be equal to the power absorbed by the grid, that is:

$$\left(I_{dc} - sC_{dc}U_{dc}\right)U_{dc} = \sum_{k=a,b,c} V_{ik}(s) * i_k(s) \tag{12}$$

3.2 VSG Link

The implementation of VSG control requires the use of a suitable inverter control structure. Commonly used control methods are P/Q control, V/F control and Droop control. VSG control algorithms can be divided into two main categories, which are described below:

P/Q control, composed of an outer power loop and an inner current loop, can realize the constant power output of the distributed generator. P/Q control is widely used in grid-connected VSG units. When P/Q control is applied in grid-connected mode, the active power can obey the governor's scheduling command well.

V/F control can output a constant voltage and frequency. This control method is more common when the island VSG. The VSG achieves amplitude control of the voltage by simulating the excitation

regulation of the SG. The output voltage is adjusted according to the VSG output voltage deviation and the voltage regulation capability is characterized by a voltage regulation factor. Fig. 3 is the active power and reactive power control block diagram of the VSG.

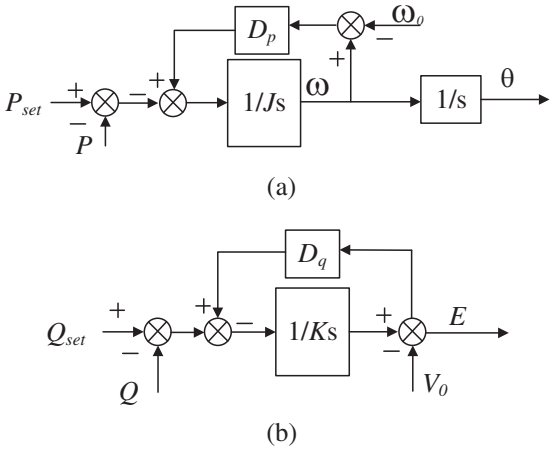

Figure 3: VSG control (a) active power control (b) reactive power control

It has been found that there is a strong coupling effect between the frequency f_p and its complementary frequency $2f_1 - f_p$ in voltage source converter (VSC) [40,41], where f_1 is the fundamental frequency. If a disturbance voltage is applied to the VSC, the stimulated current not only contains components of the same frequency but also components of complementary frequencies.

Using the frequency convolution theorem, power in the frequency domain can be obtained:

$$P_e[f] = \begin{cases} 1.5V_1I_{dr} & dc \\ 3\left(V_1I_p + V_1I_n + I_1^*V_p + I_1V_n\right) & f = \pm fp \end{cases} \tag{13}$$

$$Q_e[f] = \begin{cases} -1.5V_1I_{qr} & dc \\ 3\left(\pm jV_1I_p \mp jV_1I_n - I_2^*V_p - I_2V_n\right) & f = \pm fp \end{cases} \tag{14}$$

where $I_2 = (I_1/2)\, e^{\pm j\left(\varphi_{i1} - \pi/2\right)}$, $I_{dr} = I_1 \cos\varphi_{i1}$, and $I_{qr} = I_1 \sin\varphi_{i1}$

In Fig. 3, θ and E_m can be obtained according to the VSG active and reactive power controller.

$$\theta = \frac{1}{Js^2 + D_ps}\left(\omega_nD_p + \frac{P_{set}}{\omega_n} - \frac{P_e}{\omega_n}\right) \tag{15}$$

$$E_m = \frac{1}{Ks + D_q}\left(Q_{set} - Q_e\right) + V_0 \tag{16}$$

Substituting Eqs. (13) and (14) into Eqs. (15) and (16). θ and E_m in frequency can be obtained as Eqs. (17) and (18).

$$\theta[f] = \begin{cases} \dfrac{1}{Js^2 + D_ps}\left[\omega_nD_p + \dfrac{P_{set}}{\omega_n} - \dfrac{1.5V_1I_{dr}}{\omega_n}\right] & dc \\ \dfrac{-3}{\omega_n}\dfrac{1}{Js^2 + D_ps}\left(V_1I_p + V_1I_n + I_1^*V_p + I_1V_n\right) & f = \pm f_p \end{cases} \tag{17}$$

$$E_m[f] = \begin{cases} V_0 & dc \\ -3D(s)\left(\pm jV_1I_p \mp jV_1I_n - I_2^*V_p - I_1V_n\right) & f = \pm f_p \end{cases} \tag{18}$$

The output reactive power of the voltage-controlled VSG is determined by the voltage amplitude difference on the filter inductor L_f. Usually, the value L_f is small, so the voltage amplitude difference on it is small. In addition, the voltage fluctuation of the output terminal of the voltage-controlled VSG is also small and thus E_m can be considered a constant when modelling small signals. The positive and negative sequence impedances of the voltage-controlled VSG are shown in Appendixes A1 and A2.

The voltage-current loop controlled by VSG is shown in Fig. 4. E is the voltage modulated by the reactive power loop, K_{pv} is the proportional adjustment coefficient of the voltage loop, K_{pc} and K_{ic} are the proportional and integral coefficients of the current loop respectively. K_d is the decoupling term. The double closed-loop control method is adopted, which can track the voltage and current components of the dq axis timely and accurately, so it has good transient characteristics.

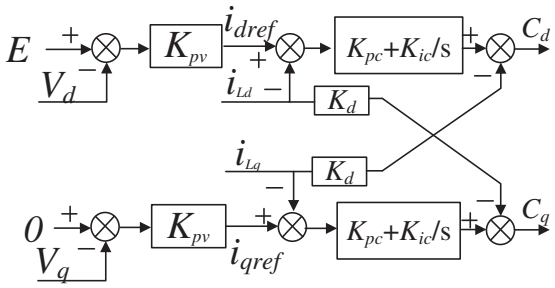

Figure 4: Voltage and current double closed loop

In Fig. 4, the modulation through the voltage and current double loops can be obtained as:

$$\begin{cases} C_d = G_i(s)\left(i_{dref} - i_{Ld}\right) - K_d i_{Lq} \\ C_q = G_i(s)\left(i_{qref} - i_{Lq}\right) - K_d i_{Ld} \end{cases} \tag{19}$$

where $G_i(s)$ is the transfer function of PI control in current regulator.

When a phase angle disturbance occurs in the PLL, $\Delta\theta \neq 0$, the output voltage and current of the voltage-controlled VSG in the dq coordinate system can be obtained as:

$$V_d[f] = \begin{cases} V_1 & dc \\ V_p + V_n & f = \pm f_p \end{cases} \tag{20}$$

$$V_q[f] = \begin{cases} 0 & dc \\ \mp jV_p \pm jV_n - \dfrac{3V_1}{\omega_n}\dfrac{1}{Js^2 + D_p s} & \\ \left(V_1I_p + V_1I_n + I_1^*V_p + I_1V_n\right) & f = \pm fp \end{cases} \tag{21}$$

$$I_d[f] = \begin{cases} I_1\cos\varphi_{i1} & dc \\ I_p + I_n + \dfrac{3I_{qr}}{\omega_n}\dfrac{1}{Js^2 + D_p s} & \\ \left(V_1I_p + V_1I_n + I_1^*V_p + I_1V_n\right) & f = \pm f_p \end{cases} \tag{22}$$

$$I_q[f] = \begin{cases} I_1 \sin \varphi_{i1} & dc \\ \mp jI_p \pm jI_n + \dfrac{3I_{dr}}{\omega_n} \dfrac{1}{Js^2 + D_p s} & \\ \left(V_1 I_p + V_1 I_n + I_1^* V_p + I_1 V_n\right) & f = \pm f_p \end{cases} \tag{23}$$

Integrating Eqs. (20)–(23), C_{dq} in frequency domain are shown in Appendixes A3 and A4, The sequence component of positive is taken at the same time, finally, the output impedance expression can be obtained in Appendixes A5–A8.

The admittance matrix can be obtained by impedance.

$$\begin{bmatrix} Y_{pp} & Y_{pn} \\ Y_{np} & Y_{nn} \end{bmatrix} = \begin{bmatrix} \dfrac{Z_{nn}}{Z_{pp}Z_{nn} - Z_{pn}Z_{np}} & \dfrac{-Z_{pn}}{Z_{pp}Z_{nn} - Z_{pn}Z_{np}} \\ \dfrac{-Z_{np}}{Z_{pp}Z_{nn} - Z_{pn}Z_{np}} & \dfrac{Z_{pp}}{Z_{pp}Z_{nn} - Z_{pn}Z_{np}} \end{bmatrix} \tag{24}$$

3.3 Model Analysis of VSG

Fig. 5 is the Bode diagram of the VSG positive sequence impedance, the parameters are shown in Table 2. The moment of inertia J and the droop coefficient D_p are enlarged and reduced by 10 times, respectively. The comparison shows that J has a great effect on the phase margin, and the selection range J is not large for the low frequency, considering the stability margin. The droop coefficient D_p mainly affects the impedance characteristics near the fundamental frequency. The larger D_p is, the closer the VSG will be to the capacitance characteristics. The quantity in the high frequency range presents capacitive characteristics. It can lead to problems with the stability of VSG operation.

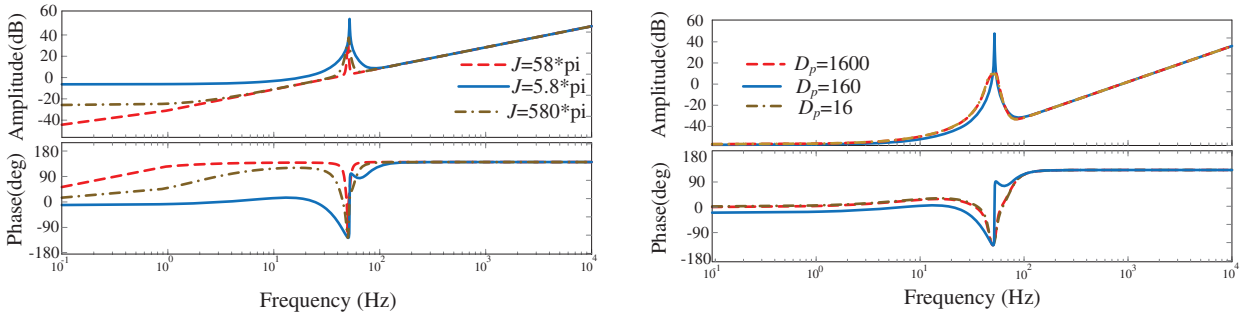

Figure 5: VSG positive sequence impedance bode. (a) VSG positive sequence impedance when J changes (b) VSG positive sequence impedance when D_p changes

Table 2: VSG impedance parameters

Parameter	Value	Parameter	Value
f_1/Hz	50	L_f/μH	8
f/kHz	10	T_s/s	1/10e3

(Continued)

Table 2 (continued)

Parameter	Value	Parameter	Value
J	5.8 ∗ pi	D_p/N·m·s	1600
w_v/rand.s	4000 ∗ 2 ∗ pi	w_i/ran.s	4000 ∗ 2 ∗ pi

The VSG output impedance can be improved by changing the parameters in the active and reactive loops, but changing the parameters of the power loop will have an impact on the dynamic stability performance of the VSG.

In Figs. 6a and 6b, J mainly affects the phase angle and amplitude of the positive sequence impedance of the VSG at low frequencies. For an excessively large J, the phase margin of the VSG impedance gradually increases. For an excessively little J, the phase angle and amplitude of the VSG impedance will change greatly at low frequencies, especially at the fundamental frequency. Therefore, there is a certain selection range for J. For the off-diagonal element Z_{np} (s), the impedance Bode plot of Z_{nn} (s) is shown in Figs. 6c and 6d. As J gradually increases, the phase margin of the VSG negative sequence impedance also increases gradually.

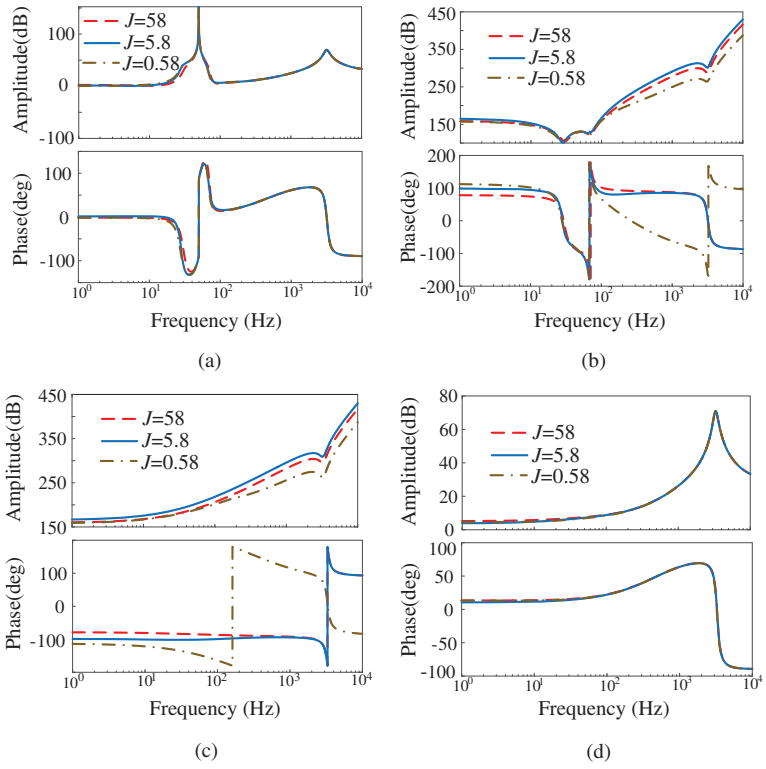

Figure 6: Bode plot of VSG output impedance during J transformation

It can be seen in Fig. 7. When K gradually increases, the larger the oscillation frequency of the response is, the better the system can suppress the shock. In the high frequency band, K is coupled with the impedance of the VSG. The larger the value K, the lower the coupling degree of the system.

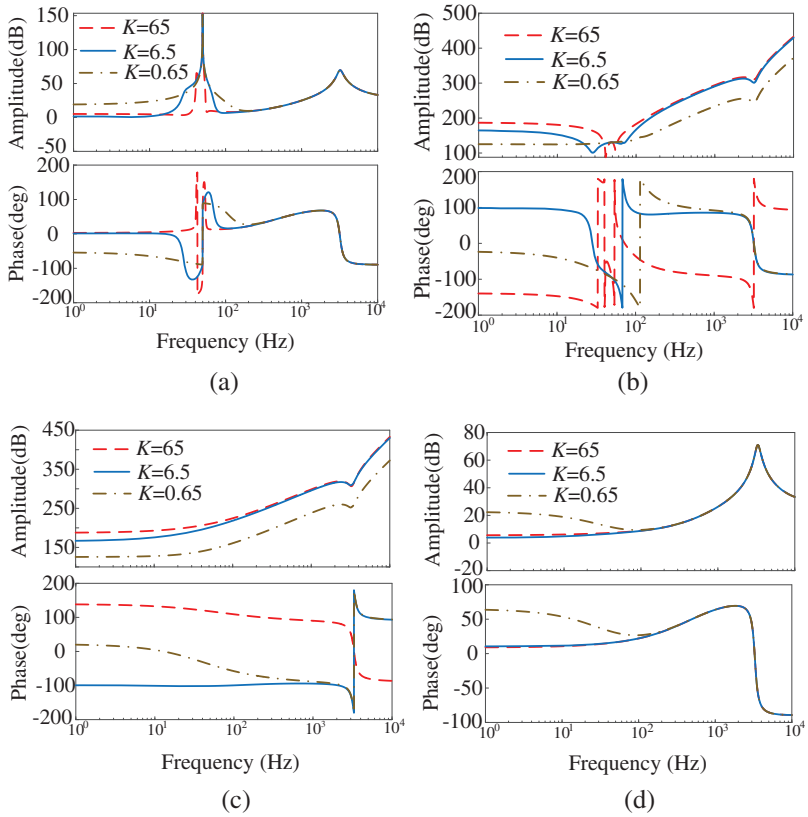

Figure 7: Bode plot of VSG output impedance during K transformation

4 Simulation Verification

In this section, the VSM-VSG collaborative control strategy was adopted, as shown in Fig. 8 which mainly includes VSM control on the machine side and VSG control on the network side.

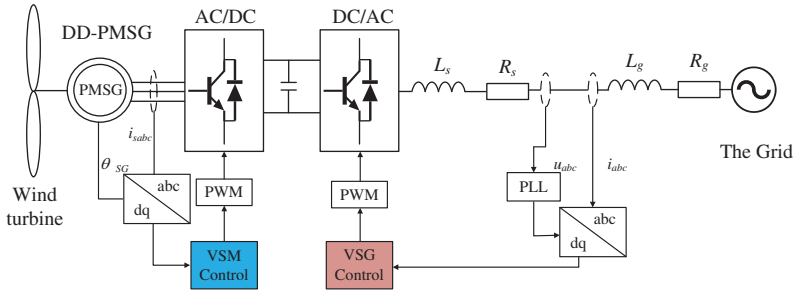

Figure 8: Control block diagram of VSM-VSG

Generally, when the SCR is 2∼3, it is a weak connection, and when the SCR is less than 2, it is a very weak connection. The connection strength to the AC grid is usually characterized by the connection reactance value. The larger the connection reactance, the weaker the AC system strength, the lower the SSO frequency, the weaker the damping, and the higher the risk of unstable SSO in the system.

The system model shown in Fig. 8 is built in MATLAB/Simulink, and the system parameters are shown in Table 3. The main validation in this paper is the effectiveness of the suppression strategy so that the natural variation in wind speed is not reflected.

Table 3: Type IV wind power model system parameters

Parameter	Value	Parameter	Value
P_o/kW	1500	U_g/V	380
Q_{ref}/Kvar	0	X_L/H	0.506
P_{ref}/kW	1500	X_C/F	2.05e-06
f/Hz	50	C_{dc}/F	0.003
C_{dc}/F	0.002	L_g/mH	80
U_{dc}/V	600	C/μF	10

The improved control block diagram is shown in Fig. 9. The wind turbine system is connected to the power grid through a power electronic converter. The MSC is generally used to control the maximum output power, and the GSC is used to control the DC bus voltage. Currently, converters are mainly vector controlled in the dq coordinate system. However, due to the coupling terms related to the system parameters in the decoupling process, the vector control method is sensitive to the changes in grid LCL filter system parameters. VSG control can be well applied to the back-to-back converter. The converter on the wind turbine side absorbs power from the permanent magnet synchronous generator (PMSG) and feeds it into the DC bus, so that it can operate in virtual synchronous motor (VSM) mode. Different from the vector control, the synchronous converter control strategy does not depend on the parameters of the PMSG, so it can improve the system's performs well. The VSG algorithm is used to control the Type IV WTGs.

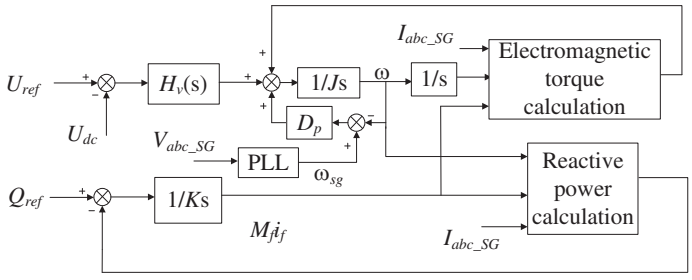

(a)

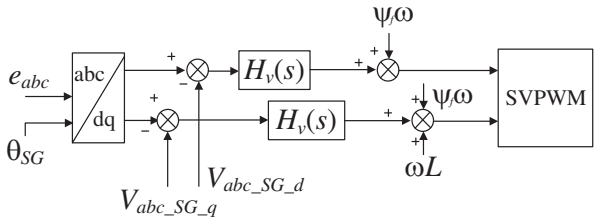

(b)

Figure 9: (Continued)

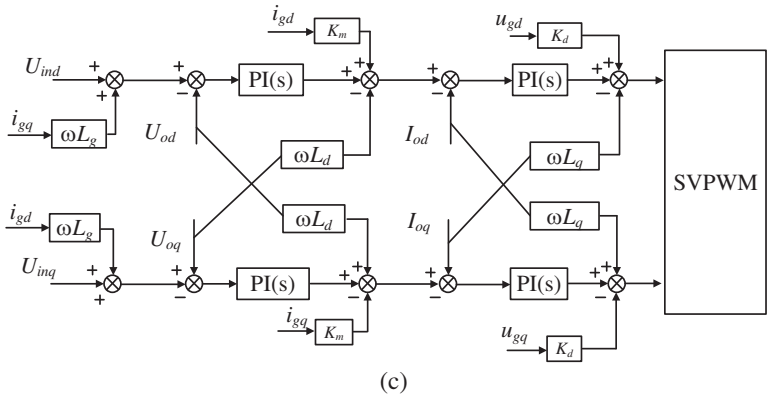

(c)

Figure 9: 9 VSG control block diagram. (a) DC voltage regulation control (b) voltage control (c) improved voltage and current double loop

The voltage and current of the system simulation are shown in Fig. 10. The system is connected to the grid through the PLL at 1 s, and the power oscillation at the subsynchronous frequency occurs. Fig. 10a shows that the voltage occurs SSO within 1.45–1.5 s after grid connection, and gradually converges. During the occurrence of SSO, the waveform is seriously distorted. In the weak grid environment, the current contains a large number of harmonics, and the wave distortion is 14.36%.

Fig. 11 shows the grid integration of active and reactive power. From Fig. 11a, it can be seen that the active power has a large shock at grid connection, after which there is a periodic oscillation around 0, after which it slowly converges, but the oscillation time is long. From Fig. 11b, it can be seen that reactive power has a shock at 0.5 s. After that, the reactive power is negative, indicating that the grid is absorbing capacitive reactive power. At this time, the grid is capacitive and will form coupling with the grid inductance. This causes oscillation and affects the stability of the system.

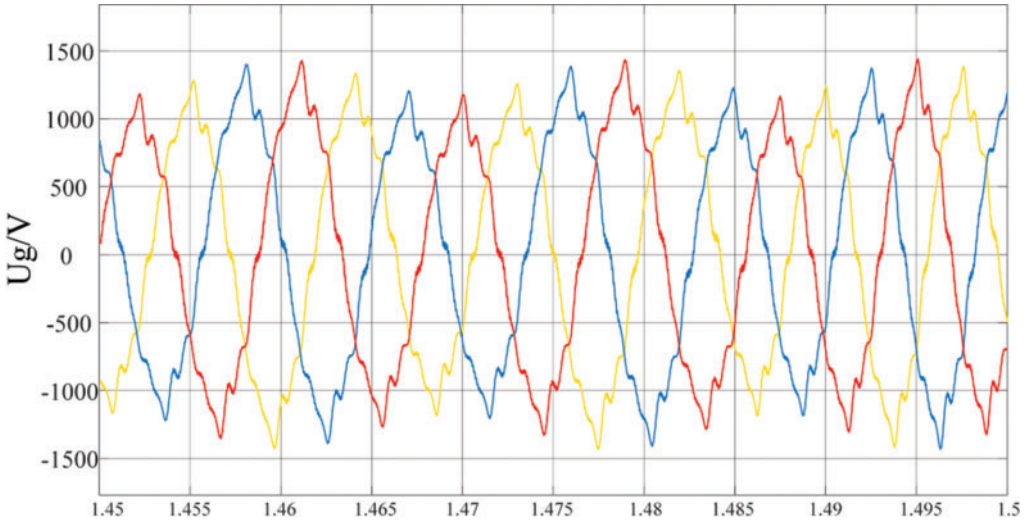

(a)

Figure 10: (Continued)

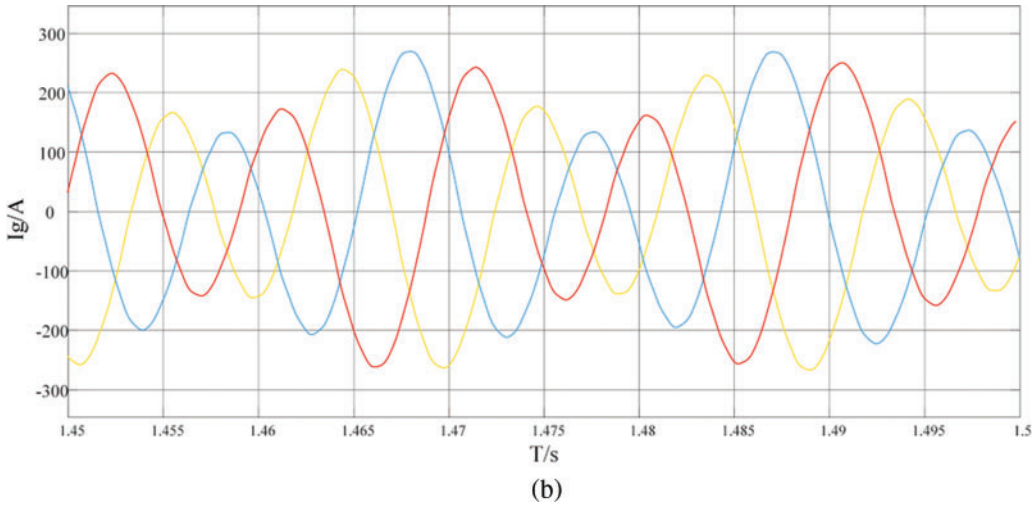

Figure 10: Grid-connected waveform. (a) voltage (b) current

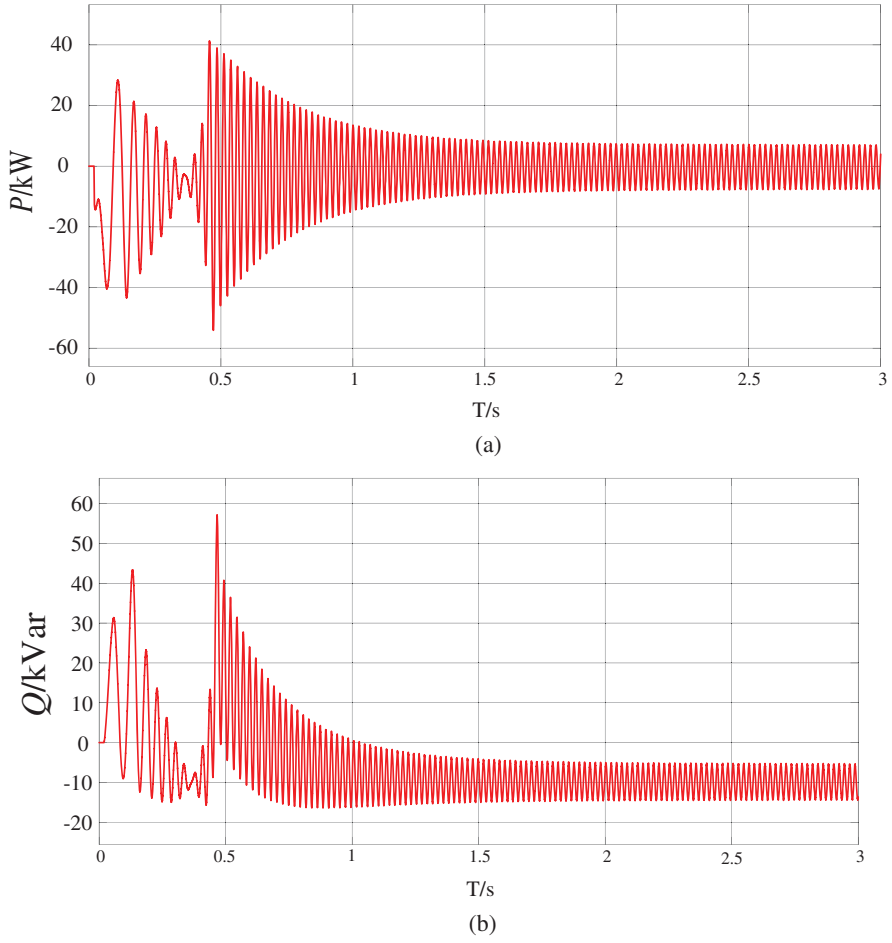

Figure 11: Oscillation power waveform. (a) active power (b) reactive power

Mainly to stabilize the DC voltage, DC voltage stabilization control was added at the front end of the active control link. The impact of DC voltage disturbance was fatal for the grid side, meanwhile, we modelized the active link of VSG to design the active power control and introduced the sag factor and rotational inertia as a way to stabilize the system.

The electromagnetic effect of the synchronous motor was taken into account in the reactive link and introduced the excitation current $M_f i_f$ as a way to better simulate the operating characteristics of the SG. The reactive voltage sag factor is introduced to give the turbine side the ability to stabilize in case of faults.

The unimproved control strategy is unable to balance the coupling of the RSC and GSC voltage and current loop dq axes. The original controls did not take into account the grid voltage and current too, resulting in large grid current harmonics. To balance the dq axis voltage and current, the control algorithm shown is adopted on the grid side.

To verify the effectiveness of the control method, the voltage and current control are built in MATLAB/Simulink as shown in Fig. 9. The rest of the simulation conditions are the same.

The active power and reactive power are obtained as shown in Fig. 12. It can be seen that before 0.3 s, the power will still oscillate with amplitude reaching 500 kW. After 0.3 s, the system gradually stabilizes and the power fluctuates slightly.

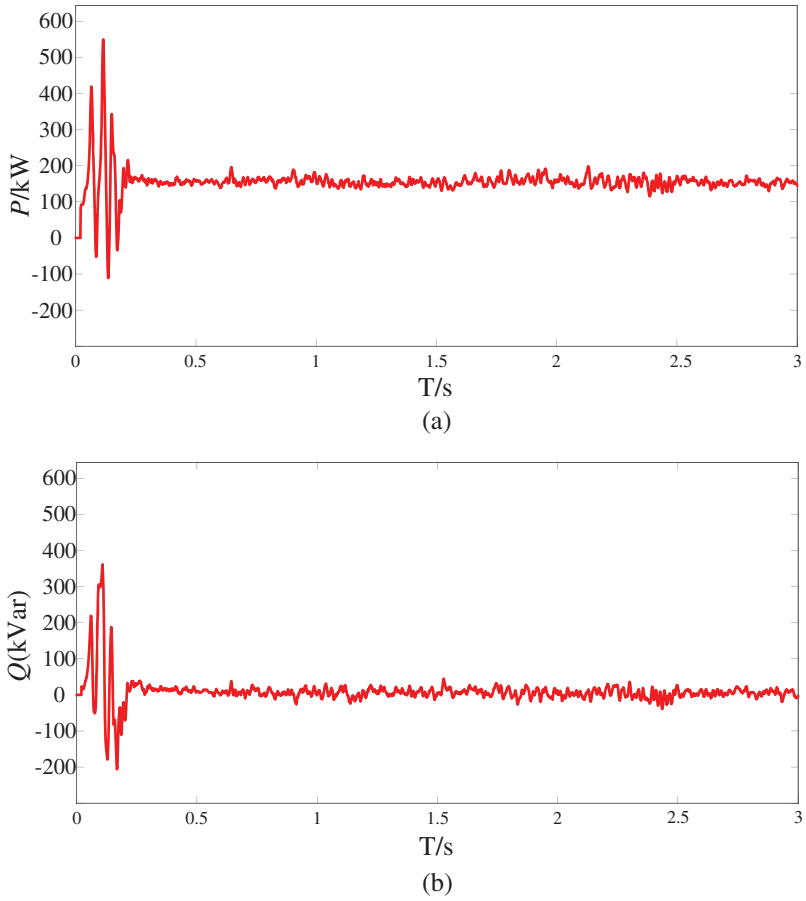

Figure 12: Power with improved control. (a) active power (b) reactive power

Fig. 13 shows the improved voltage waveform. The system operates in a very weak grid (SCR = 1.615) before 1.5 s, and the system has SSO that lasts for nearly 1 s, thus the grid voltage contained a large number of harmonics. The total harmonic of the wave distortion rate reached 13.67%, and then the waveform gradually approached the sine wave, and the system gradually stabilized. Afterwards, the system was operated under a weak grid (SCR = 2.15). It can be seen that the improved control method has a significant suppression effect on the SSO in the weak grid and can effectively suppress the harmonics of the grid voltage. Moreover, the harmonic distortion rate is 0.02%. As shown in Fig. 14. When the system is under normal strength (SCR = 4.6), due to the decrease in line impedance, the amplitude of grid voltage increases, which can meet the requirements of grid connection.

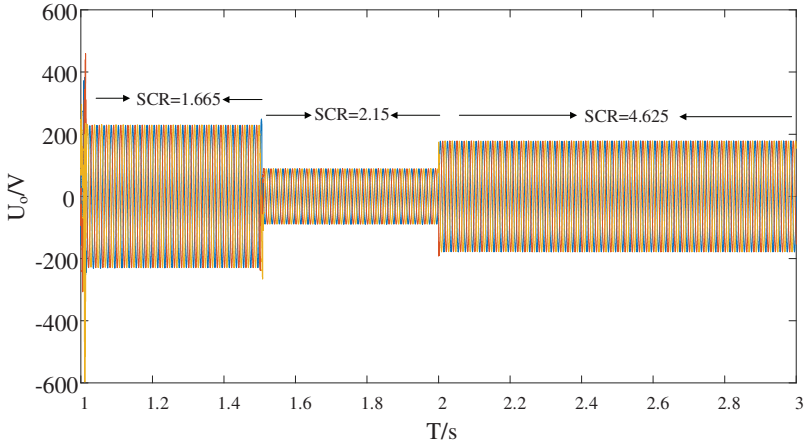

Figure 13: Voltage with improved control

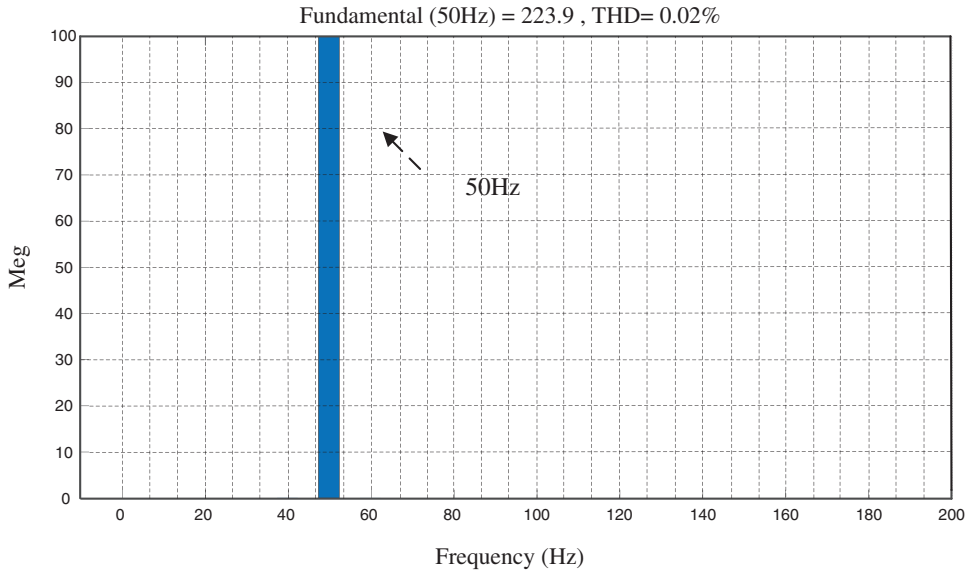

Figure 14: FFT analysis of voltage

5 Conclusion

In this paper, a Type IV WTG is built to interconnect the system with the grid. The frequency-coupled impedance model of the VSG and VSG are developed by using impedance analysis methods. Improvements are made to the voltage and current dual loop to balance the dq component coupling. The control parameters of the VSG are analyzed and compared. The influence of the rotational inertia J and the voltage factor K on the system is investigated. It was found that:

(1) The turbine-side section is controlled by VSG with the addition of a voltage regulator module. Modification of PLL control parameters usually has a limited effect on the system impedance.

(2) For double closed-loop systems, J and K affect the phase and amplitude near the VSG fundamental frequency. The selection of a smaller J system will have fluctuations on the phase; at high frequencies, K couples the VSG impedance and K affects the coupling of VSG systems. The higher the K value, the lower the system coupling.

(3) The unbalanced double closed-loop system generates currents and voltages containing a large number of harmonics. The control strategy investigated is to add the grid voltage dq component to the GSC side for modulation. At the same time, the current inner loop is coupled in the dq axis in a balanced manner. This suppression strategy provides a good solution for the effect of SSO on grid connection, which can effectively suppress the effect of sub-synchronous frequency and reduce the harmonics of grid voltage and current.

The goal of this paper is to analyze and suppress SSO in weak grids, but the interaction between sub/super-synchronous and low frequency oscillations can be found in many fields today. Because of the above situation, research and analysis are still critical and urgent. This includes the impact of distributed power plants at different locations and the adaptive regulation of control systems.

Acknowledgement: None.

Funding Statement: The author received no specific funding for this study.

Author Contributions: The authors confirm contribution to the paper as follows: study conception and design: Chongyang Zhao; data collection: Lin Chen; analysis and interpretation of results: Chongyang Zhao, Wei Chai, Beibei Rui; draft manuscript preparation: Wei Chai. All authors re viewed the results and approved the final version of the manuscript.

Availability of Data and Materials: The authors confirm that the data supporting the findings of this study are available within the article and/or its supplementary materials.

Conflicts of Interest: The authors declare that they have no conflicts of interest to report regarding the present study.

References

1. National Bureau of Statistics (2020). Statistical bulletin of national economic and social development. www.stats.gov.cn/sj/zxfb/202302/t20230228_1919011.html
2. Wu, H., Ruan, X. B., Yang, D. S., Chen, X. R., Zhao, W. X. et al. (2016). Small-signal modeling and parameters design for virtual synchronous generators. *IEEE Transactions on Industrial Electronics, 63(7),* 4292–4303.
3. Shintai, T., Miura, Y., Ise, T. (2014). Oscillation damping of a distributed generator using a virtual synchronous generator. *IEEE Transactions on Power Delivery, 29(2),* 668–676.

4. Liu, J., Miura, Y., Ise, T. (2016). Comparison of dynamic characteristics between virtual synchronous generator and droop control in inverter-based distributed generators. *IEEE Transactions on Power Electronics, 31(5),* 3600–3611.
5. Fathi, A., Shafiee, Q., Bevrani, H. (2018). Robust frequency control of microgrids using an extended virtual synchronous generator. *IEEE Transactions on Power Systems, 33(6),* 6289–6297.
6. Zhong, Q. C., Phi-Long, N., Ma, Z. Y., Sheng, W. X. (2014). Self-synchronized synchronverters: Inverters without a dedicated synchronization unit. *IEEE Transactions on Power Electronics, 29(2),* 617–630.
7. Wang, F., Zhang, L. J., Feng, X. Y., Guo, H. (2018). An adaptive control strategy for virtual synchronous generator. *IEEE Transactions on Industry Applications, 54(5),* 5124–5133.
8. Damas, R. N., Son, Y., Yoon, M., Kim, S. Y., Choi, S. (2020). Subsynchronous oscillation and advanced analysis: A review. *IEEE Access, 8,* 224020–224032.
9. Xiao, X. N., Zhang, J., Gao, B. F., Wu, Y. S., Luo, C. et al. (2013). Simulation and study on mitigation measures of frequent subsynchronous oscillation with low amplitude at multi-power plants. *Science China Technological Sciences, 56(10),* 1340–1353.
10. Luiz, A. S. P., Willis, F. L., Abdel-Aty, E. (2001). Basic mechanisms of control interactions among power electronic-assisted power systems. *IEEE/PES Transmission and Distribution Conference and Exposition. Developing New Perspectives, 1,* 397–402.
11. Liu, H. K., Xie, X. R., He, J. B., Xu, T., Yu, Z. et al. (2017). Subsynchronous interaction between direct-drive PMSG based wind farms and weak AC networks. *IEEE Transactions on Power Systems, 32(6),* 4708–4720.
12. Shair, J., Xie, X. R., Li, Y. H., Terzija, V. (2021). Hardware-in-the-loop and field validation of a rotor-side subsynchronous damping controller for a series compensated DFIG system. *IEEE Transactions on Power Delivery, 36(2),* 698–709.
13. Guo, J., Chen, Y. D., Wang, L., Wu, W. H., Wang, X. Y. et al. (2021). Impedance analysis and stabilization of virtual synchronous generators with different DC-link voltage controllers under weak grid. *IEEE Transactions on Power Electronics, 36(10),* 11397–11408.
14. Rafique, Z., Khalid, H. M., Muyeen, S. M., Kamwa, I. (2022). Bibliographic review on power system oscillations damping: An era of conventional grids and renewable energy integration. *International Journal of Electrical Power & Energy Systems, 136,* 107556.
15. Yuan, Q., Wen, X., Li, W., Renbo, W., Hao, L. et al. (2020). Subsynchronous oscillation monitoring and alarm method based on phasor measurements. *Global Energy Interconnection, 3(5),* 464–474.
16. Abdeen, M., Li, H., Jing, L. (2020). Improved subsynchronous oscillation detection method in a DFIG-based wind farm interfaced with a series-compensated network. *International Journal of Electrical Power & Energy Systems, 119(1),* 105930.
17. Farahani, M. (2012). A new control strategy of SMES for mitigating subsynchronous oscillations. *Physica C: Superconductivity, 483,* 34–39.
18. Gil-Gonzalez, W., Montoya, O. D., Garces, A. (2018). Control of a SMES for mitigating subsynchronous oscillations in power systems A PBC-PI approach. *Journal of Energy Storage, 20,* 163–172.
19. Haris, M. K., Farid, F., Magdi, S. M., Mutaz, H. (2023). Wide area monitoring system operations in modern power grids: A median regression function-based state estimation approach towards cyber attacks. *Sustainable Energy, Grids and Networks, 34,* 101009.
20. Li, P., Xiong, L., Ma, M., Huang, S., Zhu, Z. (2022). Energy-shaping L2-gain controller for PMSG wind turbine to mitigate subsynchronous interaction. *International Journal of Electrical Power & Energy Systems, 135,* 0142–0615.
21. Li, P., Xiong, L., Ma, M., Huang, S., Zhu, Z. (2022). Energy-shaping L2-gain controller for PMSG wind turbine to mitigate subsynchronous interaction. *International Journal of Electrical Power & Energy Systems, 135,* 0142–0615.

22. Kumar, S., Kumar, N., Jain, V. (2012). Comparison of various auxiliary signals for damping subsynchronous oscillations using TCR-FC. *Energy Procedia, 14,* 695–701.
23. Ghorbani, A., Pourmohammad, S. (2011). A novel excitation controller to damp subsynchronous oscillations. *International Journal of Electrical Power & Energy Systems, 33(3),* 411–419.
24. Liu, Y. Q., Zheng, J. Y., Chen, Q. C., Duan, Z. Y., Tian, Y. H. et al. (2022). MMC-STATCOM supplementary wide-band damping control to mitigate subsynchronous control interaction in wind farms. *International Journal of Electrical Power & Energy Systems, 141,* 108171.
25. Li, G. X., Chen, Y. D., Luo, A., Wang, Y. C. (2021). An inertia phase locked loop for suppressing subsynchronous resonance of renewable energy generation system under weak grid. *IEEE Transactions on Power Systems, 36(5),* 4621–4631.
26. Fan, L. L., Miao, Z. X. (2018). Wind in weak grids: 4 Hz or 30 Hz oscillations? *IEEE Transactions on Power Systems, 33(5),* 5803–5804.
27. Li, Y., Fan, L. L., Miao, Z. X. (2020). Wind in weak grids: Low-frequency oscillations, subsynchronous oscillations, and torsional interactions. *IEEE Transactions on Power Systems, 35(1),* 109–118.
28. Khalid, H. M., Peng, J. C. H. (2016). Tracking electromechanical oscillations: An enhanced maximum-likelihood based approach. *IEEE Transactions on Power Systems, 31(3),* 1799–1808.
29. Khalid, H. M., Peng, J. C. H. (2015). Improved recursive electromechanical oscillations monitoring scheme: A novel distributed approach. *IEEE Transactions on Power Systems, 30(2),* 680–688.
30. Wu, X., Xu, S. S., Shi, X. Y., Shahidehpour, M., Wang, M. T. et al. (2023). Mitigating subsynchronous oscillation using model-free adaptive control of DFIGs. *IEEE Transactions on Sustainable Energy, 14(1),* 242–253.
31. Yang, S. H., Shen, R. X., Shu, J., Zhang, T., Li, Y. J. (2022). PLL based sub-/super-synchronous resonance damping controller for D-PMSG wind farm integrated power systems. *IEEE Transactions on Energy Conversion, 37(4),* 2370–2384.
32. Shair, J., Xie, X. R., Yang, J. J., Li, J. Y., Li, H. Z. (2022). Adaptive damping control of subsynchronous oscillation in DFIG-based wind farms connected to series-compensated network. *IEEE Transactions on Power Delivery, 37(2),* 1036–1049.
33. Verma, P., Seethalekshmi, K., Dwivedi, B. (2022). A self-regulating virtual synchronous generator control of doubly fed induction generator-wind farms. *IEEE Canadian Journal of Electrical and Computer Engineering, 46(1),* 35–43.
34. Mohammed, N., Meng, K., Xiao, W. D., Al-Durra, A., Dong, Z. Y. (2023). Online grid impedance estimation-based adaptive control of virtual synchronous generators considering strong and weak grid conditions. *IEEE Transactions on Sustainable Energy, 14(1),* 673–687.
35. Ambia, M. N., Meng, K., Xiao, W. D., Al-Durra, A., Dong, Z. Y. (2021). Interactive grid synchronization-based virtual synchronous generator control scheme on weak grid integration. *IEEE Transactions on Smart Grid, 13(5),* 4057–4071.
36. Zhang, X. Y., Liu, H. Z., Fu, Y., Li, Y. G. (2022). Virtual shaft control of DFIG-based wind turbines for power oscillation suppression. *IEEE Transactions on Sustainable Energy, 13(4),* 2316–2330.
37. Zhang, F., Li, J. X., Liu, J., Gao, W. Z., He, J. G. (2023). An improved interpolated DFT-based parameter identification for sub-/super-synchronous oscillations with synchrophasors. *IEEE Transactions on Power Systems, 38(2),* 1714–1727.
38. Xue, T., Lyu, J., Wang, H., Cai, X., Li, J. Y. et al. (2020). A complete impedance model of a PMSG-based wind turbine system considering machine-side dynamics. *The 46th Annual Conference of the IEEE Industrial Electronics Society*, Singapore.
39. Shi, K., Wang, Y., Sun, Y. X., Xu, P. F., Gao, F. (2021). Frequency-coupled impedance modeling of virtual synchronous generators. *IEEE Transactions on Power Systems, 36(4),* 3692–3700.

40. Liu, H. C., Sun, J. (2014). Voltage stability and control of offshore wind farms with AC collection and HVDC transmission. *IEEE Journal of Emerging and Selected Topics in Power Electronics, 2(4),* 1181–1189.
41. Shu, D. W., Xie, X. R., Rao, H., Gao, X. D., Jiang, Q. R. et al. (2018). Sub- and super-synchronous interactions between STATCOMs and weak AC/DC transmissions with series compensations. *IEEE Transactions on Power Electronics, 33(9),* 7424–7437.

Appendix A

$$Z_{vp}(s) = \left[\frac{3V_1}{4\omega_n} M(s - j2\pi f_1) K(s) e^{j\varphi_{vir}} + sL_f\right] * \left[1 + \frac{3I_1}{4\omega_n} M(s - j2\pi f_1) K(s) e^{j\varphi_{vir}}\right]^{-1} \tag{A1}$$

$$Z_{vn}(s) = \left[\frac{3V_1}{4\omega_n} M(s + j2\pi f_1) K(s) e^{-j\varphi_{vir}} + sL_f\right] * \left[1 + \frac{3I_1}{4\omega_n} M(s + j2\pi f_1) K(s) e^{j(-\varphi_{vir})}\right]^{-1} \tag{A2}$$

where ω_v and ω_i are the cut-off angular frequency of the low-pass filter of the voltage and current signals, respectively, T_s is the switching period. Remaining parameters are listed in Table 1.

$$C_d[f] = \begin{cases} -G_i(s) I_{dr} - K_d I_{qr} - G_i(s) Y_c(s) V_1 & dc \\ \left\{\left[-3D(s) B - V_p - V_n\right] k_{pv} - I_p - I_n + \dfrac{3M(s) I_{qr} A}{\omega_n}\right\} G_i(s) & \\ -K_d\left[\mp jI_p \pm jI_n + \dfrac{3M(s) I_{dr} A}{\omega_n}\right] - G_i(s) Y_c(s)\left(V_p + V_n\right) & \\ -K_d Y_c(s)\left[\dfrac{3V_1 M(s) A}{\omega_n} \mp jV_p \pm jV_n\right] & f = \pm f_p \end{cases} \tag{A3}$$

$$C_q[f] = \begin{cases} -G_i(s) I_{qr} + K_d I_{dr} + K_d Y_c(s) V_1 & dc \\ \left\{\left[-\dfrac{3M(s) V_1 A}{\omega_n} \pm jV_p \mp jV_n\right] k_{pv} \pm jI_p \mp jI_n - \dfrac{3M(s) I_{dr} A}{\omega_n}\right\} G_i(s) & \\ -G_i(s) Y_c(s)\left[\mp jV_p \pm jV_n + \dfrac{3V_1 M(s) A}{\omega_n}\right] + K_d Y_c(s)\left(V_p + V_n\right) & \\ +K_d\left[-\dfrac{3M(s) I_{qr} A}{\omega_n} + I_p + I_n\right] & f = \pm f_p \end{cases} \tag{A4}$$

$$Z_{pp}(s)=\left\{\begin{array}{l}\left[\dfrac{-j3k_{pv}G_i(s-j\omega_1)\,V_1M(s-j\omega_1)}{2\omega_n}-\dfrac{j3k_{pv}G_i(s-j\omega_1)\,D(s-j\omega_1)}{2}\right]\\ \times V_1-G_i(s-j\omega_1)+jK_d-L_f(s+j\omega_1)\end{array}\right\}$$
$$\times\left[\begin{array}{l}\dfrac{-j3k_{pv}G_i(s-j\omega_1)\,V_1M(s-j\omega_1)}{2\omega_n}I_1^*+\dfrac{3k_{pv}G_i(s-j\omega_1)\,D(s-j\omega_1)}{2}I_2^*-k_{pv}G_i(s-j\omega_1)\\ -G_i(s-j\omega_1)\,Y_c(s+j\omega_1)+jK_dY_c(s+j\omega_1)-Z_f(s+j\omega_1)\end{array}\right]^{-1}\tag{A5}$$

$$Z_{pn}(s)=\left\{\left[\frac{-\mathrm{j}3k_{pv}G_i(s-j\omega_1)\,V_1M(s-j\omega_1)}{2\omega_n}+\frac{\mathrm{j}3k_{pv}G_i(s-j\omega_1)\,D(s-j\omega_1)}{2}\right]V_1\right\}$$
$$\times\left[\begin{array}{l}\dfrac{-\mathrm{j}3k_{pv}G_i(s-j\omega_1)\,V_1M(s-j\omega_1)}{2\omega_n}I_1^*+\dfrac{3k_{pv}G_i(s-j\omega_1)\,D(s-j\omega_1)}{2}I_2^*\\ -k_{pv}G_i(s-j\omega_1)-G_1(s-j\omega_1)\,Y_c(s+j\omega_1)+\mathrm{j}K_dY_c(s+j\omega_1)-Z_f(s+\mathrm{j}\omega_1)\end{array}\right]^{-1}\tag{A6}$$

$$Z_{np}(s)=\left\{\left[\frac{j3k_{pv}G_i(s+j\omega_1)\,V_1M(s+j\omega_1)}{2\omega_n}-\frac{j3k_{pv}G_i(s+j\omega_1)\,D(s+j\omega_1)}{2}\right]V_1\right\}$$
$$\times\left[\begin{array}{l}\dfrac{j3k_{pv}G_i(s+j\omega_1)\,V_1M(s+j\omega_1)}{2\omega_n}I_1^*+\dfrac{3k_{pv}G_i(s+j\omega_1)\,D(s+j\omega_1)}{2}I_2^*-k_{pv}G_i(s+j\omega_1)\\ -G_i(s+j\omega_1)\,Y_c(s-j\omega_1)+jK_dY_c(s-j\omega_1)-Z_f(s-j\omega_1)\end{array}\right]^{-1}\tag{A7}$$

$$Z_{nn}(s)=\left\{\begin{array}{l}\left[\dfrac{j3k_{pv}G_i(s+j\omega_1)\,V_1M(s+j\omega_1)}{2\omega_n}+\dfrac{j3k_{pv}G_i(s+j\omega_1)\,D(s+j\omega_1)}{2}\right]V_1\\ -G_i(s+j\omega_1)+jK_d-L_f(s-j\omega_1)\end{array}\right\}$$
$$\times\left[\begin{array}{l}\dfrac{j3k_{pv}G_i(s+j\omega_1)\,V_1M(s+j\omega_1)}{2\omega_n}I_1^*+\dfrac{3k_{pv}G_i(s+j\omega_1)\,D(s+j\omega_1)}{2}I_2^*-k_{pv}G_i(s+j\omega_1)\\ -G_1(s+j\omega_1)\,Y_c(s-j\omega_1)+jK_dY_c(s-j\omega_1)-Z_f(s-j\omega_1)\end{array}\right]^{-1}\tag{A8}$$